Low friction and wear resistant coatings

Carvalho, Nuno Jorge Marcolino

5

CHARACTERISATION OF TiN AND TiN/(Ti,Al)N MULTILAYERS

5.1 INTRODUCTION

Transition metal nitrides have been studied intensively in the last decades due to their properties and are today widely used. Titanium nitride belongs to the group of so-called hard refractory metals. They are characterised by having a high melting point (1500 - 3400 °C), hardness (20 - 30 GPa), brittleness, and metallic conductivity.[1] The bonding structure of these hard metals consists of a combination of localised metal-to-metal and metal-to-nonmetal interactions resembling both covalent and metallic bonding.[2] The metal-to-nonmetal bonding is favoured by the octahedral grouping of the metal atoms around a central carbon or nitrogen atom, however, the presence of the nonmetal also tends to increase the strength of metal-to-metal bonds. There also exists an electronic charge transfer from the metal to the nonmetal atoms, being greater in the nitrides than in the carbides, i.e., with increasing electronegativity of the nonmetal atom.[3] Thus, the bonding arises from simultaneous contributions of covalent, metallic, and ionic bonding to the cohesive energy.[4]

The Ti-N equilibrium phase diagram shows three stable solid phases. The cubic B1-NaCl crystal structure δ-TiN phase is stable over a wide composition range $(0.6 < N/Ti < 1.2)$ and the hexagonal α-Ti phase can dissolve up to 15 at.% nitrogen. The ε-Ti_2N crystallises in a tetragonal structure and exists only at a

composition range of 33 at.%.[1] However, it is the cubic δ-TiN phase that is mostly used in technological applications. Stoichiometric, as well as off-stoichiometric, polycrystalline films have been deposited by a variety of techniques including reactive dc,[5] rf,[6] magnetron sputtering,[7] activated reactive evaporation,[8] and triode ion plating (e-gun) with high plasma density.[9] However, the observed physical properties of these films are reported to vary over orders of magnitude, depending on both the growth technique and the particular deposition parameters.

During the last decade there has been an increasing interest in TiN because of the successful use in a variety of thin film applications. For example, its high hardness gives a good resistance to abrasive wear, and the high chemical stability results in a high resistance to solution wear. Therefore, it is particularly useful for increasing the wear resistance of high speed steel cutting tools, punches and metal forming components.[10,11] In addition, due to the good corrosion and erosion resistance, relative inertness, high sublimation temperature, optical and electronic properties, TiN coatings also have been considered for applications, such as diffusion barriers in microelectronic devices,[12] cosmetic gold-coloured surfaces,[13] and wavelength-selective transparent optical films.[14]

Even though titanium nitride coatings have already a dominant position, still considerable efforts are invested in the research and development of multilayer coatings to further enhance the wear resistance of coated components. By alternately depositing two (or more) chemically and/or mechanically different materials, the stress concentration and the conditions for crack propagation can be changed. The multilayer structure may act as a crack inhibitor and thereby increasing the coating fracture resistance. This effect is suggested to result from crack deflection due to weak interfaces,[15] crack tip shielding by plastic deformation in combination with strong interfaces,[16] a favourable residual stress distribution,[17] and crack deflection due to a large differences in stiffness between the individual layer materials.[18] Moreover, the properties of the surface can be improved by the deposition of layers that separately have different kinds of effects on the surface, such as corrosion protection, wear protection, thermal isolation, electrical conductivity, diffusion barrier, and adhesion to the substrate.

Coatings comprising many thin layers of TiN and titanium aluminium nitride ((Ti,Al)N)) take advantage of the multilayer properties and the properties of each component. The primary advantage of (Ti,Al)N is its higher oxidation resistance at elevated temperatures. TiN oxidises rapidly at temperatures above ~600 ^{o}C to form TiO_2. Because of the large difference in molar volumes between the TiO_2 and TiN, compressive stresses are developed in the oxide layer resulting in its spallation.[19] On the other hand, (Ti,Al)N forms a dense, highly adhesive Al_2O_3 layer on top of the coating protecting it from further oxidation. The oxide layer has demonstrated to be effective in decreasing the interdiffusion of oxygen and aluminium in the coating.[20] Accordingly, the diffusion wear, one of the major wear mechanisms on cutting tools, is reduced. Moreover, its lower thermal conductivity prompts more heat to be dissipated via chip removal, permitting higher cutting speeds due to lower thermal loading on the substrate.[21]

Understanding the physical properties, such as the mechanical response, of such complex nonhomogeneous materials requires a detailed knowledge of the microstructure. This chapter presents the results of an investigation on TiN and TiN/(Ti,Al)N multilayers deposited onto stainless steel and tool steel substrates.

5.2 SUBSTRATE MATERIALS AND METHODS OF CHARACTERISATION

Two different materials, one cold work tool steel (AISI D2) and one stainless steel (AISI 304), with dimension 90x10x1.5 mm were used as substrate for both coatings. The chemical compositions (other than iron) and hardness of the substrate materials are as follows. For AISI D2 (wt.%): 1.55 C, 0.3 Si, 0.4 Mn, 11.8 Cr, 0.8 Mo, 0.8 V, hardness 6.8 GPa; for AISI 304 (wt.%): max 0.08 C, 1.0 Si, 19.0 Cr, 2.0 Mn, 10.0 Ni, hardness 1.6 GPa. The tool steel was heat treated and tempered at 520 ^{o}C to obtain the above mentioned hardness. All substrates were polished to mirror finish, corresponding to R_a values of approximately 0.05 μm. Total coating thickness determination was performed by direct measurements on polished or fractured cross-sections using scanning electron microscopy (SEM). The thickness of the individual layers were measured on cross-sectional

transmission electron microscopy specimens. The coatings structure was determined by x-ray diffraction (XRD) measurements in Bragg-Brentano geometry. Microchemical analyses were performed by energy dispersive x-ray spectroscopy (EDS) using the focused electron probe of a transmission electron microscope. The focused electron probe - having a nominal probe diameter of 1.0 nm FWHM - was scanned over the surface of a cross-sectional specimen to obtain the elemental line profile distribution. The microstructure of the as-deposited coatings was studied by plan-view and cross-sectional transmission electron microscopy (TEM).

5.3 CRYSTAL STRUCTURE AND RESIDUAL STRESS STATE

Typical XRD diffraction patterns from TiN and TiN/(Ti,Al)N deposited onto stainless steel and bare substrate are shown in figure 5.1. The substrate displays mainly reflections from the α-Fe and γ-Fe phases. TiN coatings are polycrystalline exhibiting diffraction peaks related to cubic δ-TiN phase. However, apparently the peaks have shifted towards lower diffracting angles with respect to their nominal ASTM positions. In fact, the interplanar spacing d_{hkl} for the reflecting planes parallel to the surface determined from the XRD spectra shows, irrespectively of the substrate material, higher values than those from a randomly oriented strain-free standard sample, where d_{111}=0.2449 nm. The value obtained for the (111) planes of TiN onto stainless steel and TiN onto tool steel is 0.2464 nm and 0.2461 nm, respectively. This indicates that the coating is in a state of compressive stresses, which is in agreement with previous results on deposition of TiN.[22] Textural analyses were performed using Eq. (2.1) with $I_{(hkl)}$ values determined from the integrated intensity of each (hkl) reflection and $I_{0\,(hkl)}$ values obtained from the JCPDS data of TiN. The outcome revealed that the homogeneous coating displays a strong preferred (111) orientation parallel to the substrate surface. The presence of this texture is not surprising since the (111) plane in the TiN is the one of lowest strain energy due to anisotropy in Young's modulus.[23] Therefore its alignment normal to the growing direction will minimise the total energy under strain energy dominated growth.

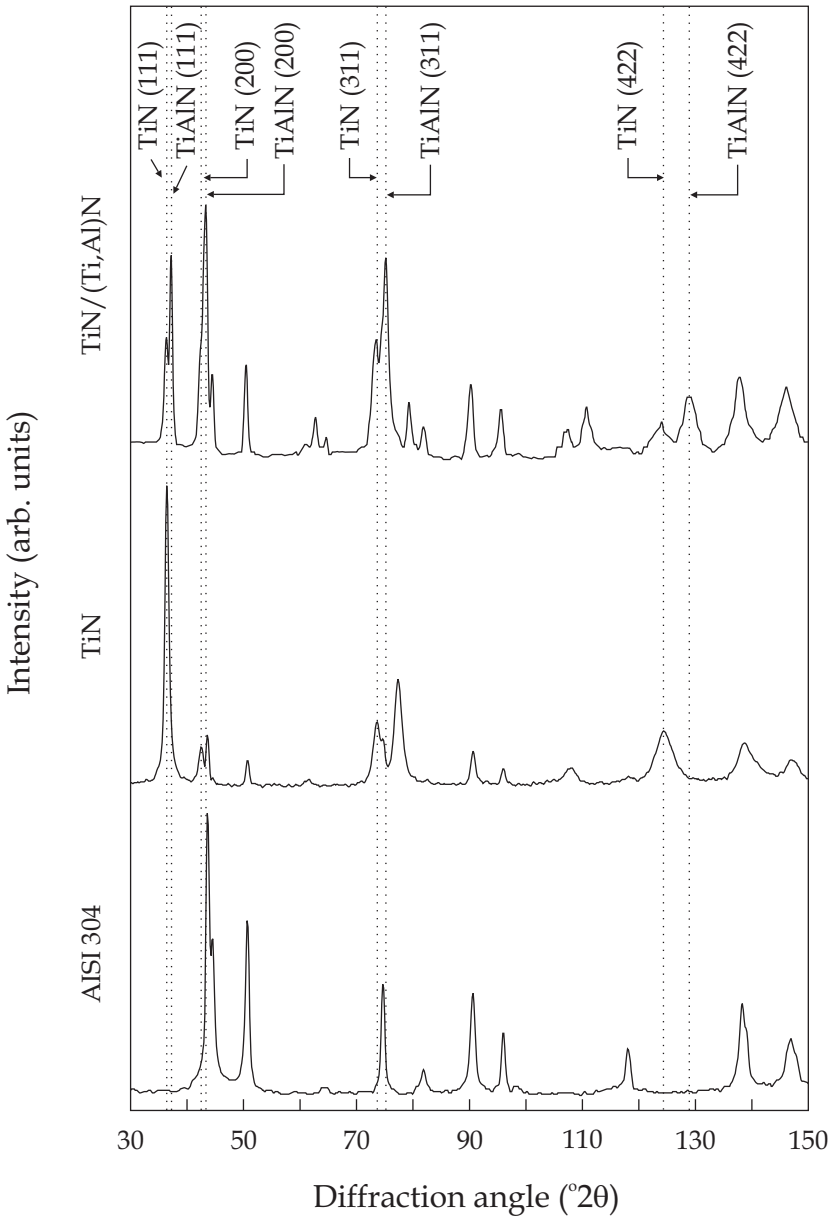

Figure 5.1 *X-ray diffraction patterns of the TiN/(Ti,Al)N multilayers (top), TiN single layer (middle), and bare substrate AISI 304 (bottom).*

The TiN and (Ti,Al)N layers from the multilayer coating also exhibited the B1-NaCl crystal structure. As seen in figure 5.1, the (Ti,Al)N peaks are shifted to lower interplanar spacing values with respect to the TiN peaks. The smaller lattice parameter is due to the titanium atoms of the TiN lattice being replaced

by aluminium atoms. Since the aluminium atomic radius is smaller than the Ti, the TiN cell is increasingly reduced with higher aluminium content until the ratio of Al to Ti exceeds the limit of approximately 1.1.[24] The small difference in interplanar spacing between TiN and (Ti,Al)N layers makes it very difficult to perform accurate textural analyses using the same method as for homogeneous TiN. Nevertheless, previous XRD polar texture scan measurements have demonstrated that both layers are slightly textured with a (311) preferred orientation.[25] As the multilayers were deposited onto two substrates, the difference in residual stresses made it possible to calculate the Poisson's ratio, the stress-free lattice parameter, and consequently, the residual stresses of the individual layers. Tables 5.1 and 5.2 summarises the results on lattice strain and macro stresses measurements performed previously.[25]

Table 5.1 *Poisson's ratio and lattice parameter of TiN and (Ti,Al)N.*

Coating	ν	a_0 [Å]
TiN	0.232±0.002	4.243±0.001
(Ti,Al)N	0.177±0.003	4.170±0.005

Table 5.2 *Residual stresses [GPa], with* $E = 450$ GPa.

Substrate	TiN	Multilayer	
		TiN	(Ti,Al)N
Stainless steel	-5.6±0.1	-10.1±0.3	-4.2±0.2
Tool steel	-4.2±0.2	-8.0±0.4	-2.7±0.1

Using the stress-free lattice parameter of (Ti,Al)N, and the lattice parameters of titanium nitride and aluminium nitride, it was possible to estimate the composition of the layers assuming that *Vegard's* rule is applicable, resulting in a chemical composition of $Ti_{0.41\pm0.04}Al_{0.59\pm0.04}N$. The disparity in the magnitude of residual stresses between the ones deposited onto stainless steel and tool steel is explained based on the thermal expansion coefficients of the substrates, being 17.8 - 18.4x10^{-6} [K^{-1}] and 11.9 - 12.9x10^{-6} [K^{-1}], respectively. Since the thermal mismatch for stainless steel is higher ($\Delta\alpha \approx 10x10^{-6}$ [K^{-1}]), the thermally induced stress present in this system is more pronounced.

The difference in residual stress for TiN and (Ti,Al)N is thought to be a result of the atomic peening effect. In the former, energetic atoms may enhance the densification during film growth, and thus increasing the compressive stress, whilst in the latter this effect seems not to be present. The lower residual stress value obtained for the homogeneous TiN compared to the TiN layers from the multilayer correlates with the fact that the residual stress is found to decrease with increasing layer thickness.[25]

5.4 SURFACE TOPOGRAPHY AND FRACTURE MORPHOLOGY

Figure 5.2 shows representative SEM micrographs of the surface of TiN and TiN/(Ti,Al)N multilayers. Their topography is typical of ion plating and sputtering deposition processes.[26] The former produces a smoother, shallow rippled surface, being to a certain extent, independent of the substrate roughness. The coating surface deposited from the latter process is flatter with fine grains. However, it reproduces the surface topography of the underlying substrate. As can be seen in figure 5.2b, the grooves and ridges are still present. Nevertheless, the surface also displays pronounced protuberances and craters. The protuberances are droplets (macroparticles), which were incorporated during growth of the coating, and craters are caused by their debonding.

Droplets smaller than about 1 μm have a nearly spherical shape, while larger ones have a more ellipsoidal. Figure 5.3 displays the TiN/(Ti,Al)N multilayer tilted at approximately 20^{o} to the plane of the surface to obtain information from both the surface and the cross-section of the droplet and the crater. The

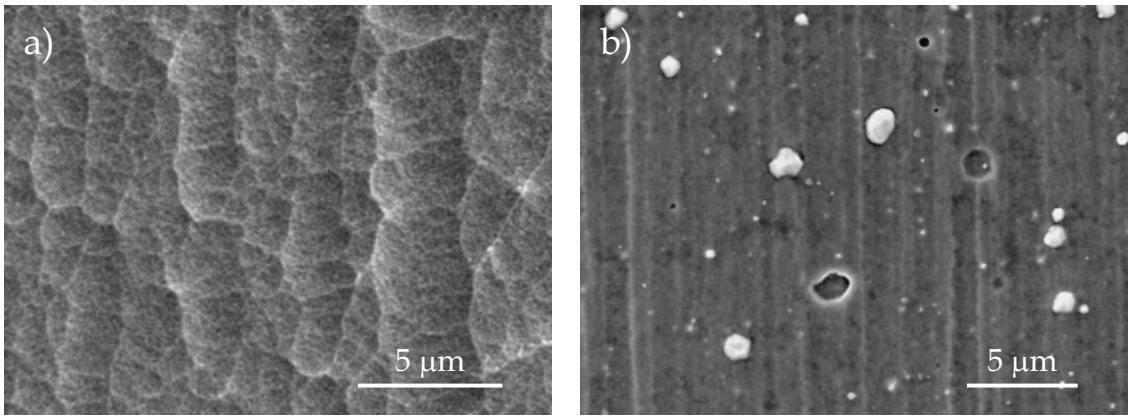

Figure 5.2 *SEM micrographs displaying the surface morphology of* (a) *TiN and* (b) *TiN/(Ti,Al)N multilayers deposited onto tool steel substrate.*

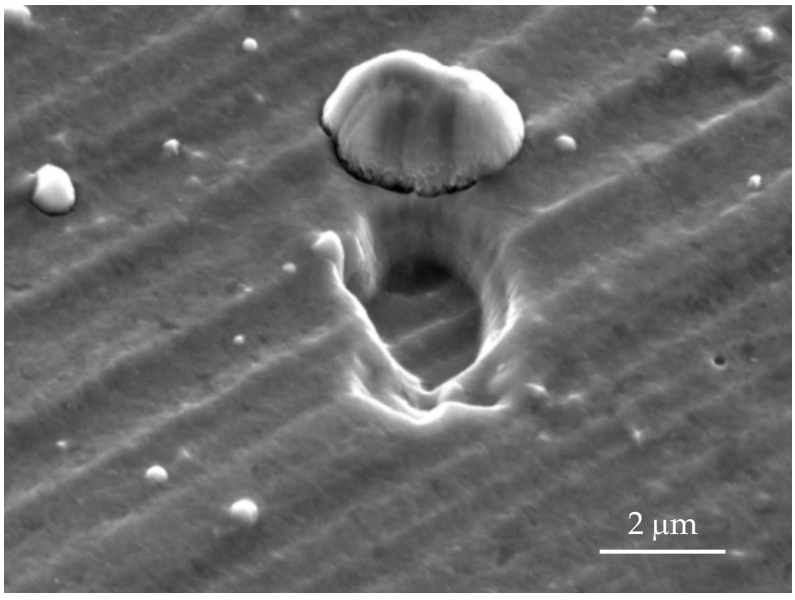

Figure 5.3 *SEM micrograph of the TiN/(Ti,Al)N multilayers showing details from both droplet and hole, which was presumably created by ejection of a droplet. The sample is tilted to allow detailed information to be retrieved.*

droplets are loosely bonded to the multilayer, as demonstrated by the crack at the rim and the morphology of the crater surface, which is similar to the coatings surface.

The morphology of the coatings is disclosed by cross-sectional SEM micrographs of fractured samples (fractographs) in figure 5.4. TiN has a densely fibrous structure typical of a zone T, according to the zone classification proposed by *Thornton*.[27] On the other hand, the TiN/(Ti,Al)N multilayers have a relatively dense structure with a more pronounced columnar microstructure, where some columns had grown from the interface up to the coating surface, possessing a structure more similar to the zone 2. Both coatings have a total thickness close to 5.0 μm and no difference between the ones deposited on tool steel and stainless steel substrates could be discerned.

Although the multilayer has been defined as a stacking of TiN and (Ti,Al)N layers, the fractograph and TEM studies (see below) exhibited the real structure, which should instead be defined as a periodical structure with the following sequence: (Ti,Al)N/(TiN/(Ti,Al)N), i.e. the multilayer is constituted of (Ti,Al)N layers and a superlattice of TiN and (Ti,Al)N. Nevertheless, for the sake of simplification, in the remaining thesis the standard designation will be adopted.

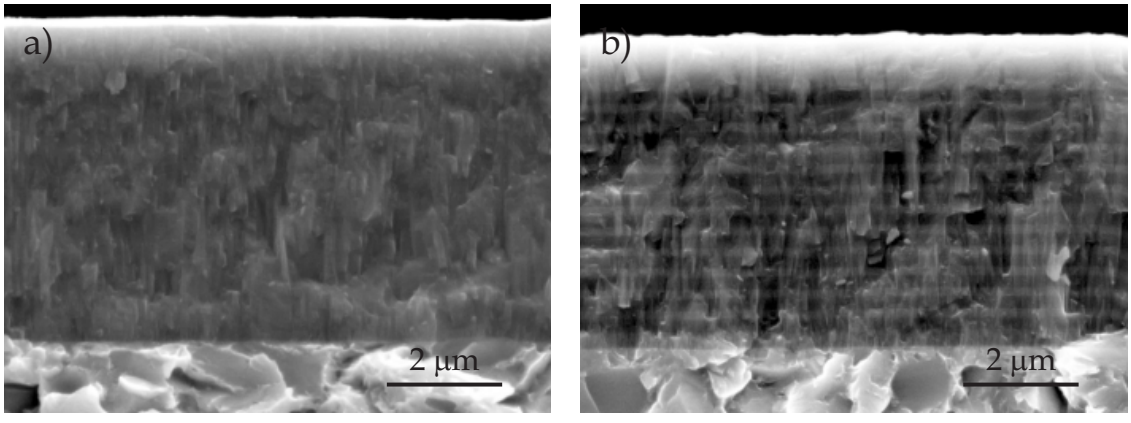

Figure 5.4 *Cross-sectional SEM micrographs of fractured samples showing the morphology of* (a) *TiN and* (b) *TiN/(Ti,Al)N multilayers. Both were deposited onto tool steel substrate.*

Figure 5.5a and 5.5b are fractured and polished cross-sectional SEM micrographs of the TiN/(Ti,Al)N multilayers, respectively. The former was obtained with a secondary electron detector, whereas the latter was obtained with a backscattered electron detector to emphasise dissimilarity between the TiN and (Ti,Al)N. TiN produces more backscattered electrons, and is therefore displayed as layers with brighter contrast. From the micrograph of the polished sample it is possible to identify a TiN interfacial layer and a (Ti,Al)N top layer. This design takes advantage of the superior properties of each constituent. TiN provides the enhanced adhesion between the coating and the substrate, which can be jeopardised if aluminium is present because of its high oxygen affinity. (Ti,Al)N protects the system from oxidation, because it has an improved resistance at a higher temperature than TiN.

All droplets analysed were found to be incorporated in the multilayer during TiN growth, and were never directly deposited on the steel substrate. Therefore, the possible formation during the cleaning and heating stages before coating deposition, as it happens whenever cathodic-arc ion etching is used, is unlikely.[28] Only the smaller droplets are covered and buried by the subsequent

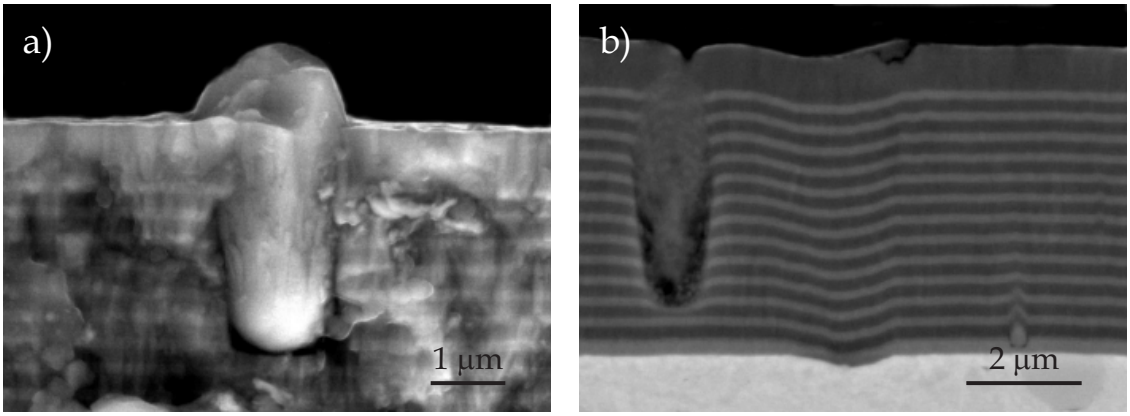

Figure 5.5 *Cross-sectional SEM micrographs of the TiN/(Ti,Al)N multilayers.* (a) *Secondary electron micrograph of fractured sample evidencing the voided region beneath the droplet.* (b) *Backscattered electron micrograph of polished sample showing the multilayers structure and the distortion caused by droplets and substrate surface irregularities.*

coating deposition leading to an undistorted surface. The wetting of droplets towards the multilayers was very poor, as shown by the near spherical bottom shape and the voids surrounding it. These findings allow to assume that, even if the droplets have left the target surface in the liquid state,[29] they have solidified *en route* due to a temperature decrease related to their diameter.[30] Consequently, they were incorporated in the multilayers in the solid state. Voids were formed because the droplets shadowed the incoming atomic flux during film growth and limited adatom mobility did not permit the growth around them.[31] The weak droplet-multilayer bonding caused by the presence of voids, results in a reduced adhesion of droplets incorporated close to the surface, leading to their easy removal on cooling from the deposition temperature because of the compressive stress in the multilayers. Therefore, the presence of craters on the surface is not surprising, as can be seen in figures 5.2b and 5.3.

5.5 MICROSTRUCTURAL FEATURES

The microstructure was investigated using transmission electron microscopy. Figures 5.6a and 5.6c are plan-view TEM images with corresponding selected area electron diffraction (SAED) patterns, taken near the coating surface. Both samples are polycrystalline with dense grain boundaries, i.e. free of intergranular porosity and cracks. This feature sometimes makes the grain boundaries difficult to discern. Therefore, one must be careful in distinguishing large grains from clusters of extremely fine grains in close crystallographic orientation. Moreover, as one column may consist of several grains or subgrains, one should be aware that the grain size can often be smaller than the column width. A high density of defects (dislocations) within the individual grains is also evident.

Moiré fringes from the TiN coating are clearly visible. Since they result from destructive interference of diffracted waves due to overlapping grains, it indicates that the TiN microstructure is more fibrous than columnar. The grain size distribution is homogeneous with an average size $\langle d \rangle$ of 50 nm. The small grain size is related to ion bombardment during film growth, which is known to create many radiation-induced defects in the growing film.[32] In the case of TiN,

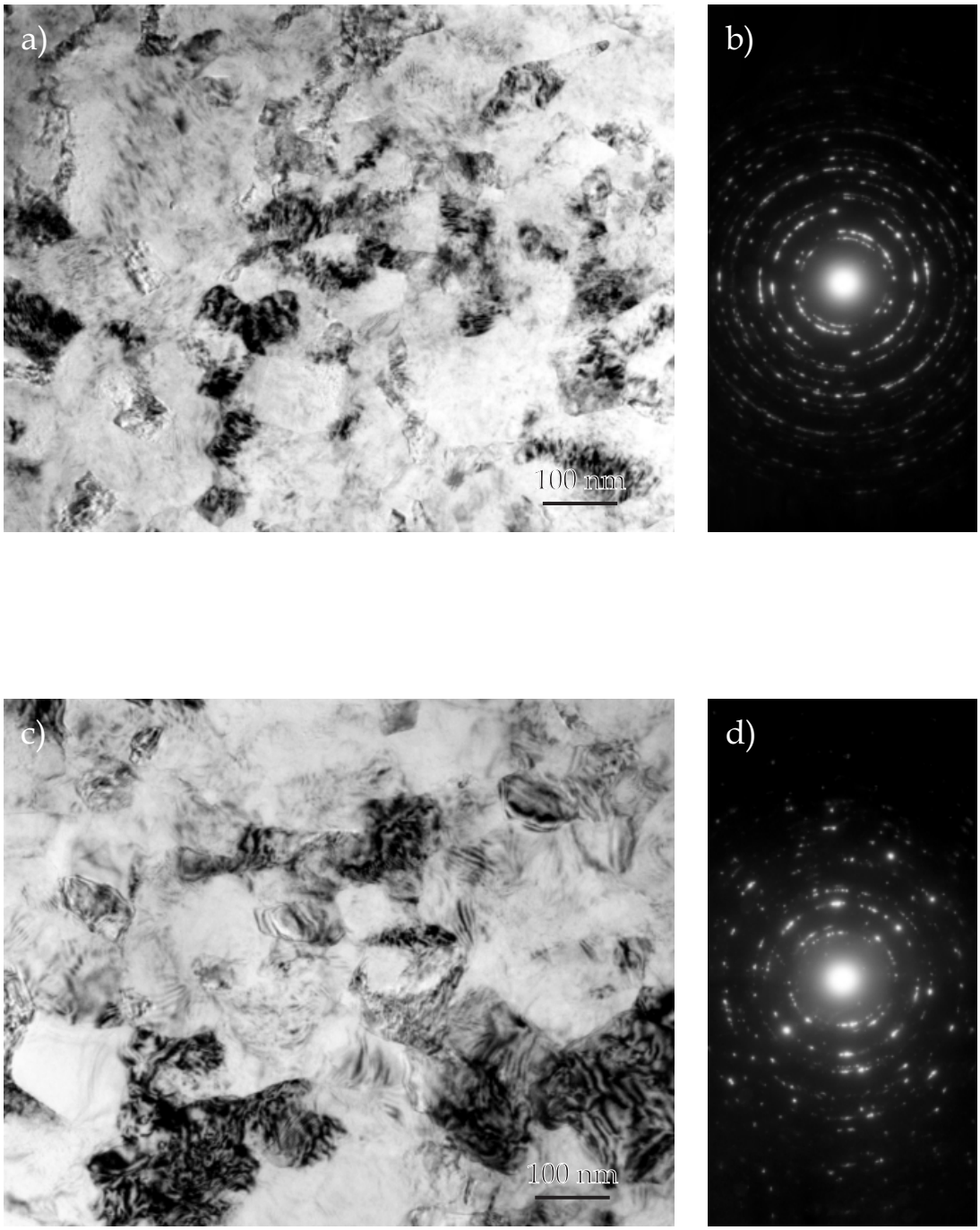

Figure 5.6 *Plan-view TEM images taken near the coating surface.* (a) *and* (c) *are the bright field images of the homogeneous TiN and the TiN/(Ti,Al)N multilayers, respectively. The electron diffraction patterns of the corresponding coatings are displayed in* (b) *and* (d).

the defect density is sufficiently large to disrupt the columnar structure, such that new columns are nucleated periodically causing the suppression of large grains.[33]

The multilayer sample exhibits coarse Moiré fringes. The effect is primarily due to beam interference from the gratings of both layers - which have a lattice mismatch of 1.6% - when they are twisted with respect to each other over a small angle. Nevertheless, although to a lesser extent than the TiN sample, there are also Moiré fringes produced from overlapping of the columnar grains. In this case, the average grain size $\langle d \rangle$ is approximately 100 nm. The twice as large grain is in conformity with the multilayer morphology. The columnar microstructure is explained as being associated to a change in nucleation and coalescence behaviour related to the multitude of different deposition process parameters.[34]

The SAED patterns in figure 5.6b and 5.6d correspond to the B1-NaCl structure. The diffraction rings from the multilayers are broader resulting from the superposition of reflections from TiN and (Ti,Al)N, where the latter has a slightly reduced lattice parameter. Also, the more diffuse diffraction rings of the homogeneous coating, in contrast to the dotted rings of the multilayers, confirms the relatively finer grain sizes and indicates a poorer crystalline perfection, i.e. the lattice distortion is retained.[35]

From plan-view TEM with SAED pattern it was possible to identify the phase of the droplets and hence their nature. Figure 5.7a is a plan-view TEM image showing a ~1 μm diameter droplet and the surrounding film. As also observed from the SEM micrographs, the droplet has a spherical geometry, minimising its surface energy, and it is loosely bonded to the surroundings. Figure 5.7b presents the SAED pattern from an area covering the core of the droplet with the $[\bar{1}12]$ zone axis, indicating that it might have the f.c.c. structure of TiN. The confirmation of the structure was obtained when tilting the specimen 20°, and the <111> zone axis was reached. This angle is unique of face centred cubic structures. Since from plan-view microscopy it is impossible to obtain depth sensitivity, it is necessary to be careful in interpreting SAED patterns from droplets that are viewed in projection. This is due of the difficulty to discern whether there is any remnant multilayer on top of it or, in fact, it is a bare

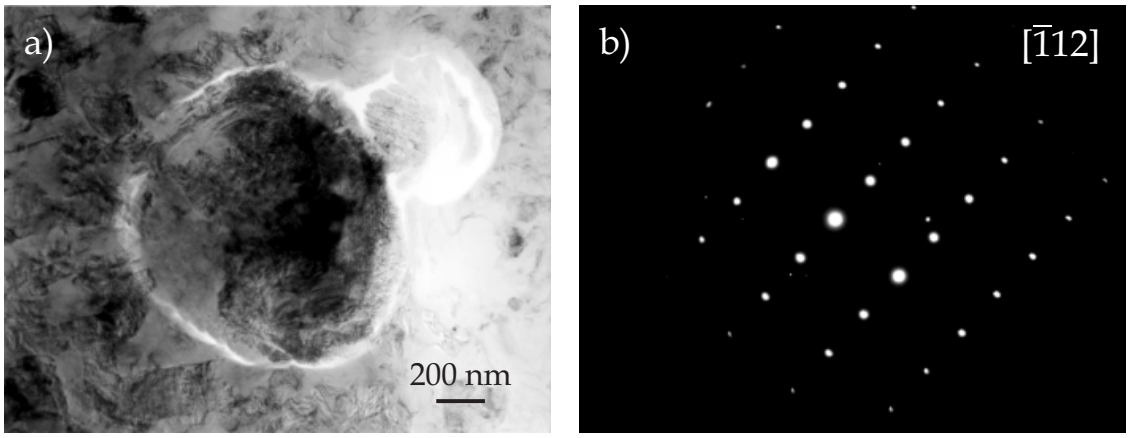

Figure 5.7 *Plan-view TEM image of a droplet incorporated in the TiN/(Ti,Al)N multilayers.* (a) *Bright-field image and* (b) *corresponding electron diffraction pattern.*

droplet which is being analysed. To cross-check its nature, orientation imaging microscopy (OIM)[36], a technique that permits to obtain Kikuchi diffraction patterns from a sample was utilised on droplets viewed in cross-section. The outcome was a Kikuchi pattern that agreed with the SAED patterns obtained. *Ljungcrantz et al.*,[30] had documented that droplets emitted from the titanium target with a composition close to pure titanium were subjected, *en route* to the substrate, to diffusion of nitrogen. However, the nitrogen pressure was not sufficient to transform the hexagonal α-Ti into cubic TiN phase. In the present study, the prospect of phase transformation during flight of the α-Ti particle to the growing film is also very unlikely due to the large particle size. However, it seems that the nitrogen pressure was high enough for nitrogen ions to be incorporated into a titanium particle at the crucible (crucible poisoning), creating a droplet that was thereafter deposited on the growing film.

Cross-sectional TEM images permitted to obtain a clear picture of the coatings microstructure, as is shown in figure 5.8a and 5.8b, and the evolution from the interface with substrate to the free surface. The fibrous structure of TiN and the columnar structure of TiN/(Ti,Al)N is clearly seen. The diameter of the former is rather difficult to calculate due to their twisted nature. It is estimated to be approximately 50 nm. The average column diameter of the latter increases with

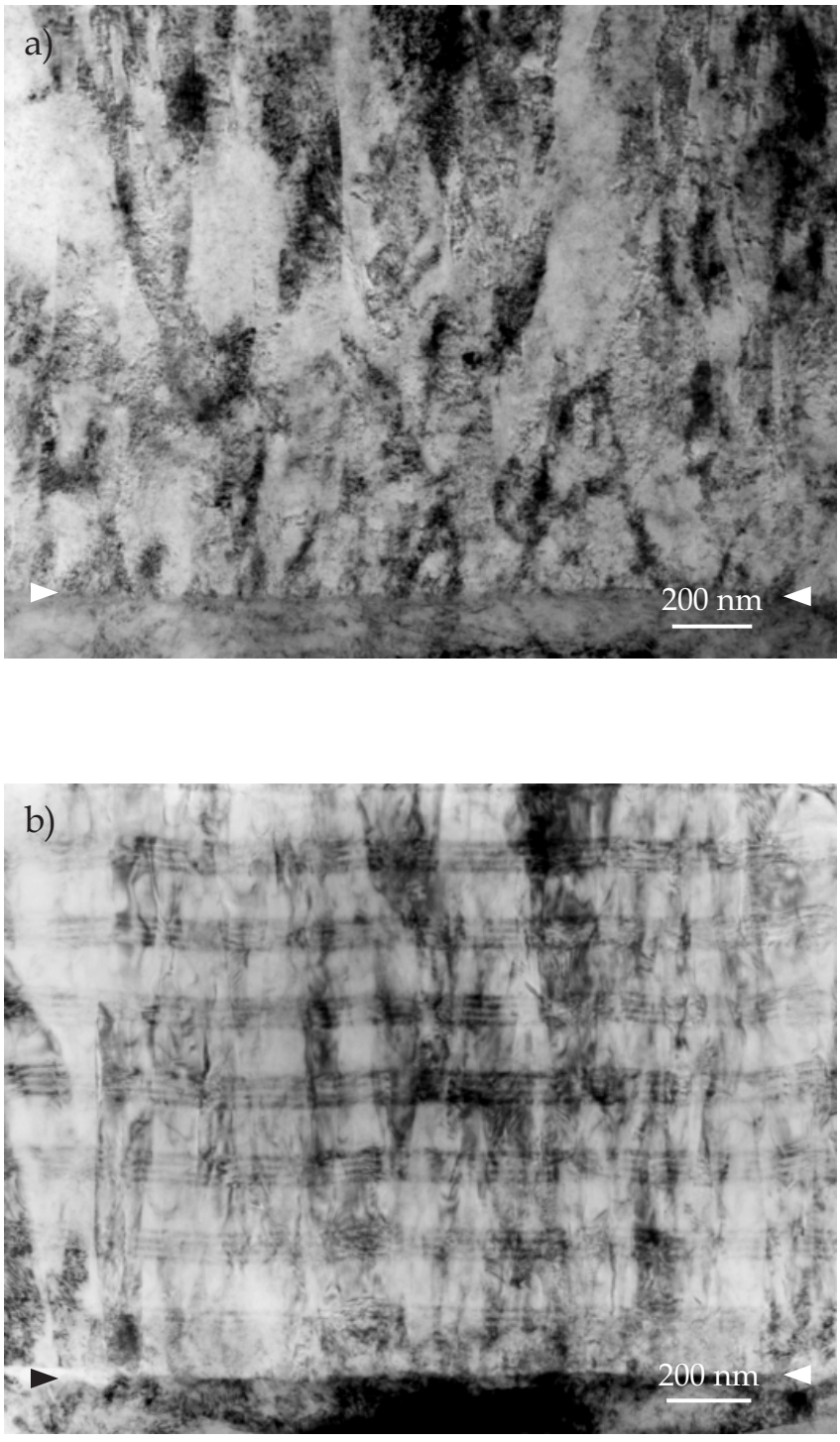

Figure 5.8 *Cross-sectional TEM images showing the near-interface microstructure of* (a) *TiN and* (b) *TiN/(Ti,Al)N multilayers grown on a stainless steel substrate. The coating-substrate interface is indicated by the arrows.*

increasing film thickness from ~80 nm at the coating-substrate interface to ~150 nm at 5 µm thickness. This indicates a continuous competition for growth among evolving columns. The grain boundaries are also more difficult to distinguish in the fibrous structure than in the columnar, indicating that the TiN film was grown with higher adatom mobility, where the primary effect is film densification by enhancing the rate at which intergranular porosity is annealed out during deposition.[37]

The influence of deposition processes on the microstructure is best seen when comparing their interfacial region, which is in both cases composed of a TiN layer and stainless steel substrate. The homogeneous TiN layer-substrate interface has an interfacial region of approximately 2 nm wherein the fibrous structure was nucleated. The columns formed in the nucleation and coalescence stages, faced severe competition from the others for survival. However, above this region (~140 nm) of tangled columns and, in some cases oversized grains, the fibrous microstructure became more uniform. This nucleation mode is commonly observed for TiN grown on stainless steel substrate due to its lack of carbides and a large lattice mismatch between the TiN and steel substrate.[33]

On the other hand, the multilayer has an abrupt interface between the TiN interlayer and the substrate. The deposition process resulted in larger initial nuclei with a more homogeneous size, which led to the formation of wider, more uniformly sized, columns that have extended throughout the entire coating. The dark contrast observed on both samples below the film-substrate interface is due to strain fields. They are associated with residual radiation-damage induced defects within the matrix of the substrate grains as a result of intense ion irradiation during ion etching.

The multilayer composition was determined by an EDS line profile using the K_α lines for the measured intensity of titanium, aluminium, and nitrogen. The sensitivity factors were calculated using the theoretical cross section method of *Zaluzec*, which is the one that gave the most reliable values. However, it should be emphasised that the concentrations presented in Figure 5.9 are considered to be semi-quantitative because no standards were used for calibration. The positions where data was taken are presented in the TEM image. The results of the analysis showed that the layers were near-stoichiometric with respect to

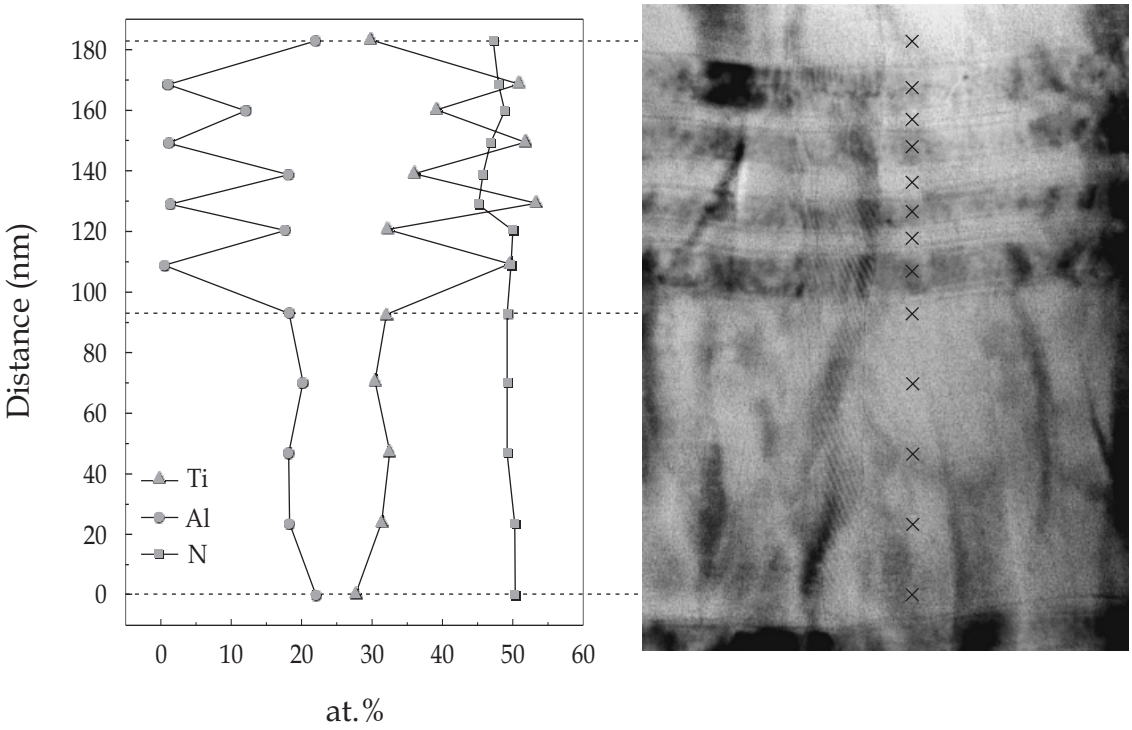

Figure 5.9 *EDS line profile across the (Ti,Al)N layer and the superlattice. Positions where data was taken are indicated in the TEM image. The nominal probe diameter was 1 nm and the spot acquisition time 30 s.*

nitrogen (i.e. Ti:N≈1:1 and (Ti,Al):N≈1:1), and that the (Ti,Al)N layers of the superlattice have practically the same composition as the thicker layer. Moreover, it is also possible to confirm that when the *Vegard's* rule is applied to thin films deposited under non-equilibrium conditions, it might lead to inaccuracies in the estimation of the composition. In this particular case, the Al concentration found was too low.

The undulation observed on the superlattice (cf. figure 5.8b) corresponds to the evolution of the columnar growth surfaces, which remarkably remains continuous across grain boundaries. Their compositional modulation was measured to be 21 nm, and found to be constant throughout the film. The TiN layer thickness to periodicity ratio of the superlattice was regular with a value of approximately 0.46. Still, occasionally the first layer of the superlattice is

broader than expected, which can be related to instabilities in the activation of the superlattice deposition.

5.6 CONCLUSIONS

The TiN and TiN/(Ti,Al)N multilayers investigated have a fibrous and columnar microstructure, respectively. The former is highly (111) textured with compressive stresses in the order of 4 to 5 GPa. The latter, is slightly (311) textured having each component a different compressive stresses, being 3 to 4 GPa for the (Ti,Al)N layer and 8 to 10 GPa for the TiN layer. There is also a compressive stress dependency on the type of substrate material, due to the thermal mismatch. The TiN/(Ti,Al)N multilayers are composed of (Ti,Al)N layers and a superlattice of TiN and (Ti,Al)N with a periodicity of 200 nm. The compositional modulation within the superlattice itself is 21 nm. Both materials have crystallised in a face centred cubic B1-NaCl structure. The lattice parameter of (Ti,Al)N was slightly reduced with respect to TiN due to the smaller atomic radius of aluminium atoms.

The microstructure and composition of micrometer-sized droplets incorporated in the multilayers during deposition of TiN material were examined. It is demonstrated that the droplets must have been ejected from the titanium source, which was nitrogen contaminated. This enhanced the nucleation of face centred cubic droplets that were subsequently solidified *en route* to the growing film. Thereafter, a voided region is formed as a consequence of shadowing of the atomic flux. As they are loosely bonded to the coating, the droplets close to surface are easily removed because of compressive stresses, leaving craters behind with exposed multilayers.

References

1. L.E. Toth, *Transition Metal Carbides and Nitrides*, Academic, New York, (1971).
2. E. Vogelzang, J. Sjollema, H.J. Boer, J.Th.M. De Hosson, J. Applied Physics **61**, 4606 (1987).

3. V. Ern, A.C. Swittendick, Physical Review **137**, 1927 (1965).
4. J.-E. Sundgren, B.O. Johansson, A. Rockett, S.A. Barnett, J.E. Greene, *Physics and Chemistry of Protective Coatings*, W.D. Sproul, J.E. Greene, J.A. Thornton (eds.), American Institute of Physics, Universal City, (1985).
5. J.M. Poitevin, G. Lemperiere, J. Tardy, Thin Solid Films **97**, 69 (1982).
6. J.-E. Sundgren, B.O. Johansson, S-E. Karlsson, Thin Solid Films **105**, 353 (1983).
7. M.K. Hibbs, B.O. Johansson, J.-E. Sundgren, U. Helmersson, Thin Solid Films **122**, 115 (1984).
8. B.E. Jacobson, R. Nimmagadda, R.F. Bunshah, Thin Solid Films **63**, 333 (1979).
9. M. Bromark, M. Larsson, P. Hedenqvist, S. Hogmark, Surf. Coatings Technol. **90**, 217 (1997).
10. R. Buhl, H.K. Pulker, E. Moll, Thin Solid Films **80**, 265 (1981).
11. R.L. Hatschek, Am. Mach. Special Report **752**, 129 (1983).
12. M. Wittmer, B. Studer, H. Melchiar, J. Applied Physics **52**, 5722 (1981).
13. B. Zega, M. Kornmann, J. Amiguet, Thin Solid Films **54**, 577 (1977).
14. E. Valkonen, T. Karlsson, B. Karlsson, B. O. Johansson, Proceedings of SPIE International Technical Conference **401**, 41 (1983).
15. K.S. Chan, M.Y. He, J.W. Hutchinsson, J. Mater. Sci. Eng. A **167**, 57 (1993).
16. Y. Huang, H.W. Zhang, Acta Metall. Mater. **41**, 1523 (1993).
17. M.Y. He, A.G. Evens, Int. J. Solids Structure **31**, 3443 (1994).
18. H. Holleck, Surf. Eng. **7**, 137 (1991).
19. U. Wahlström, L. Hultman, J.-E. Sundgren, F. Adibi, I. Petrov, J.E. Greene, Thin Solid Films **235**, 62 (1993).
20. L.A. Donohue, I.J. Smith, W.-D. Münz, I. Ptrov, J.E. Greene, Surf. Coatings. Technol. **94-95**, 226 (1997).
21. J.H. Hsieh, C. Liang, C.H. Yu, W. Wu, Surf. Coatings Technol. **108-109**, 132 (1998).
22. J.A. Thornton, J. Vac. Sci. Technol. A **4**, 3059 (1986).
23. D.R. McKenzie, Y. Yin, W.D. McFall, N.H. Hoang, J. Phys. Cond. Mater. **8**, 5883 (1996).
24. W.D. Sproul, J. Vac. Sci. Technol. A **12**, 1595 (1994).
25. E. Zoestbergen, N.J.M. Carvalho, J.Th.M. De Hosson, Surf. Engineering **17**, 1 (2001).
26. H. Randhawa, J. Vac. Sci. Technol. A **4**, 2755 (1986).
27. J.A. Thornton, Annual Review Materials Science **7**, 239 (1977).
28. I. Petov, P. Losbichler, D. Bergstrom, J.E. Greene, W.-D. Münz, T. Hurkmans, T. Trinh, Thin Solid Films **302**, 172 (1997).
29. R.L. Boxman, S. Goldsmith, Surf. Coatings Technol. **48**, 51 (1991).

30. H. Ljungcrantz, L. Hultman, J.-E. Sundgren, G. Håkansson, L. Karlsson, Surf. Coatings Technol. **63**,123 (1994).
31. J.A. Thornton, Thin Solid Films **40**, 335 (1977).
32. B.E. Jacobson, R.F. Bunshah, R. Nimmagadda, Thin Solid Films **54**,107 (1978).
33. M.K.Hibbs, B.O.Johansson, J.-E. Sundgrenm U. Helmersson, Thin Solid Films **122**, 115 (1984).
34. J.-E. Sundgren, Thin Solid Films **128**, 21 (1985).
35. D.T. Quinto, J. Vac. Sci. Technol. A **6**, 2149 (1988).
36. A.J. Schwartz, M. Kumar, B.L. Adams, *Electron Backscatter Diffraction in Materials Science*, Kluwer Academic, New York, (2000).
37. L. Hultman, G. Håkansson, U. Wahlström, J.-E. Sundgren, I. Petrov, F. Adibi, J.E. Greene, Thin Solid Films **205**, 153 (1991).